Parameter estimation for a morphochemical reaction-diffusion model of electrochemical pattern formation

Article

Accepted Version

Sgura, I., Lawless, A. S. and Bozzini, B. (2019) Parameter estimation for a morphochemical reaction-diffusion model of electrochemical pattern formation. Inverse Problems in Science and Engineering, 27 (5). pp. 618-647. ISSN 1741-5985 doi: https://doi.org/10.1080/17415977.2018.1490278 Available at http://centaur.reading.ac.uk/77573/

To link to this article DOI: http://dx.doi.org/10.1080/17415977.2018.1490278

Publisher: Taylor & Francis

Parameter estimation for a morphochemical reaction-diffusion model of electrochemical pattern formation

Ivonne Sgura[a], Amos S. Lawless [b] and Benedetto Bozzini[c]

[a] Dipartimento di Matematica e Fisica "E. De Giorgi", Università del Salento, Via per Arnesano, I-73100 Lecce, Italy;
[b]School of Mathematical and Physical Sciences, University of Reading, PO Box 220, Reading, RG6 6AX, U.K. a.s.lawless@reading.ac.uk;
[c] Dipartimento di Ingegneria dell'Innovazione, Università del Salento, via Monteroni, I-73100 Lecce, Italy benedetto.bozzini@unisalento.it

ARTICLE HISTORY
Compiled June 5, 2018

ABSTRACT

The process of electrodeposition can be described in terms of a reaction-diffusion PDE system that models the dynamics of the morphology profile and the chemical composition. Here we fit such a model to the different patterns present in a range of electrodeposited and electrochemically modified alloys using PDE constrained optimization. Experiments with simulated data show how the parameter space of the model can be divided into zones corresponding to the different physical patterns by examining the structure of an appropriate cost function. We then use real data to demonstrate how numerical optimization of the cost function can allow the model to fit the rich variety of patterns arising in experiments. The computational technique developed provides a potential tool for tuning experimental parameters to produce desired patterns.

KEYWORDS
Parameter identification; PDE constrained optimization; Reaction-diffusion PDEs; Turing pattern formation; Electrodeposition;

1. Introduction

This paper presents the first example of the fitting of an experimental electrochemical morphochemical distribution with a mathematical model of pattern formation, with corresponding parameter estimation. The pattern formation model (see below for details) is a reaction-diffusion (RD) partial differential equation (PDE) model, developed by some of the co-authors, expressing the coupling between the 3D growth morphology resulting from electrochemical phase formation and the surface chemistry controlled by electrochemical adsorption. The experimental patterns are optical and scanning electron micrographs derived from studies that have been recently published or reviewed by the authors.

In order to place our contribution in context, it is worth noting that mathematical models of

Corresponding author Email: ivonne.sgura@unisalento.it

electrochemical dynamics and of related pattern formation processes have been typically derived within the framework of activator-inhibitor mechanism in view of rationalising electrocatalytic processes [1, 2, 3]. As far as pattern formation in electrodeposition is concerned, instead, the focus has generally been on experimental aspects (e.g. [4], [5]) and, even though sophisticated physical justifications of the process have been proposed (see [6] and [7] for comprehensive reviews of this issue), no dedicated PDE-based models accounting for the actual material growth have been reported before [6]. Instead the mathematical description of these phenomena has been developed within the reaction-diffusion modelling approach, with the rather artificial ansatz of considering exclusively concentrations of the reactive species as state variables for the electrodeposition models [8]–[12], thus neglecting to describe the electrochemical phase formation process, that is the single most evident observable characterizing the process. In a series of papers developing the seminal work of [6], the reaction-diffusion modelling approach was extended by incorporating the more natural state variable representing the morphology (surface profile) together with the surface chemistry (composition) considered in as far as it controls the growth process ([13]–[21], [22] and [23]). The respective source terms represent nonlinear coupling of morphology and chemistry (morphochemical coupling) through physically transparent, classical electrokinetic, mass-transport and adsorption equations. The resulting two-variable nonlinear reaction-diffusion system - leading to the formation of Turing patterns and of transition front waves - allows us to follow accurately the phenomenology expressed in 3D electrocrystallisation. The ansatz of this specific research is this RD-PDE model, that will be employed for parameter estimation and some aspects of which are briefly summarised below.

In [6], it was shown by extensive numerical simulations that the RD-PDE model is extremely flexible in accounting for typical electrokinetic control phenomena and includes all spatio-temporal organisation forms that are known in the experimental literature. In [21] it was proved theoretically that on the one hand the RD model supports spatial pattern initiation, because of Turing's diffusion-driven instability, and on the other hand it can exhibit a variety of spatio-temporal phenomena, owing to the possibility of both transcritical and supercritical Hopf bifurcation modes. Of course, the simultaneous appearance of Turing instability, which leads to steady spatial structures, with Hopf instability, which gives rise to temporal oscillations, is of great interest because these bifurcations are responsible for the breaking of spatial and temporal symmetries, respectively. Moreover, in [21] it was shown that the spatio-temporal phenomenology occurring in the neighbourhood of a codimension-two Turing-Hopf (TH) bifurcation point [24, 25] can be further enriched as a result of a Turing-type destabilisation of the limit cycle generated by a supercritical Hopf bifurcation. In [26] this mechanism is referred to as *Turing-Hopf instability* or diffusive instability of the Hopf limit cycle and represents a different way in which Turing and Hopf instabilities can interact.

Although the properties of this model have been studied in depth in the aforementioned papers, there has been little previous work to fit such a model to the variety of electrochemical patterns arising from experiments. In a recent paper [27] the authors compared the non-stationary solutions of the RD model to experimental maps using a technique based on the Singular Value Decomposition (SVD) that estimated the optimal transient time of the model for a fixed set of parameters. In the current study we use parameter estimation techniques to provide a quantitative comparison of the RD model with stationary experimental data. Parameter estimation through optimization constrained by ODEs or PDEs is a well-established technique in many areas of science and engineering, such as oil recovery, aircraft design and environmental sciences (see, for example, [28, 29, 30] for ODEs and [31], [32], [33], [34] for PDEs). In the context of reaction-diffusion equations, such as studied here, applications of these techniques include the biological modelling of cell motility [35, 36]) and tumour growth [37]. In some bio-medical applications the parameters could also be spatially dependent functions, like in [38, 39] where the birth rate of proliferative cells in colon cancer is estimated. Recent studies on parameter estimation in the context of biological

pattern formation ([40], [41], [42]) have concentrated on development of the methodology, including demonstration of well-posedness and efficiency of solution methods. Here we apply parameter estimation methods using gradient descent algorithms in order to analyse the behaviour of our model of electrochemical pattern formation in different parameter regimes. The method developed also provides a tool that can guide the experimental design for the production of different patterns. For the purpose of this study we restrict the numerical results to stationary experimental maps, which correspond to parameters in the Turing region. This is discussed further in Section 5.

The paper is set out as follows. In the next section we discuss the RD-PDE mathematical model and discuss some of its main properties. Sections 3 and 4 describe the computational methodology for parameter estimation in the continuous and discrete frameworks. Numerical results are then presented for synthetic data in Section 5 and true data in Section 6, before we summarise the conclusions in Section 7.

2. The mathematical model

As more extensively discussed in the Introduction, the key idea behind the reaction-diffusion (RD) model proposed in [6, 21, 22], is the coupling of one equation for the morphology $\eta(x, y, t)$ with one for the surface chemistry $\theta(x, y, t)$. $\eta \in \mathbb{R}$ is adimensional and expresses the instantaneous increment of the electrodeposit thickness during the electrochemical process. The actual 3D electrodeposit morphology can be obtained as

$$h(x, y, t) = \int_0^t \eta(x, y, \tau) d\tau \quad \Leftrightarrow \quad \eta(x, y, t) = \eta_0(x, y) + \frac{dh(x, y, t)}{dt} \tag{1}$$

where $\eta_0(x, y) = \eta(x, y, 0)$ is the initial profile of the electrode.
$0 \leqslant \theta(x, y, t) \leqslant 1$ is the surface coverage with a functionally key adsorbed chemical species.
The RD-PDE system in adimensional form is given by:

$$\begin{cases} \dfrac{\partial \eta}{\partial t} = \Delta \eta + \rho f(\eta, \theta), \\[2ex] \dfrac{\partial \theta}{\partial t} = d \Delta \theta + \rho g(\eta, \theta), \end{cases} \tag{2}$$

where Δ is the two-dimensional Laplace operator, $d = D_\theta / D_\eta$ is the ratio of the diffusion coefficients for the individual chemical and morphological processes, respectively, and $\rho > 0$ is a scaling parameter playing the role of a coefficient weighting the area of the integration domain gauging the relative strength of the reaction terms (as detailed in [44]).
The nonlinear source terms that account for generation (deposition) and loss (corrosion) of the relevant material are given by

$$\begin{aligned} f(\eta, \theta) &= A_1 (1 - \theta) \eta - A_2 \eta^3 - B (\theta - \alpha), \\ g(\eta, \theta) &= C (1 + k_2 \eta) (1 - \theta) [1 - \gamma (1 - \theta)] - D (1 + k_3 \eta) \theta (1 + \gamma \theta). \end{aligned} \tag{3}$$

Model (2)-(3) is defined for $(x, y, t) \in \Omega \times [0, T]$, $\Omega = [0, L_x] \times [0, L_y]$ with L_x, L_y characteristic lengths of the electrode and T a characteristic time of the electrodeposition process. We also require

(2)-(3) to be supplemented by zero-flux boundary conditions and the following initial conditions:

$$\eta(x,y,0) = \eta_0(x,y), \qquad \theta(x,y,0) = \theta_0(x,y), \qquad (x,y) \in \Omega. \tag{4}$$

The physical meaning of the source terms (3) is briefly described here; full details are provided in [6, 21]. The term $A_1(1-\theta)\eta$ accounts for the charge-transfer rate at sites free from adsorbates; $A_2\eta^3$ describes mass-transport limitations to the electrodeposition process. The term $-B(\theta-\alpha)$ quantifies the effect of adsorbates on the electrodeposition rate. The parameter $0 < \alpha \leqslant 1$ takes into account the fact that adsorbates can have both inhibiting and enhancing effects.
The source term g can be regarded as $g(\eta,\theta) = C\, g_{ads}(\eta,\theta) - D\, g_{des}(\eta,\theta)$ such that it features adsorption (parameter C) and desorption (parameter D) terms including both chemical (expanded to second order) and electrochemical (first order) contributions.

For simplicity and without appreciable loss of generality, we make the following assumptions about parameters: (i) all the constants are taken as real positive or equal to zero, with $0 < \gamma \leqslant 1$; (ii) $k_3 < k_2$, meaning that adsorption is the dominating chemical contribution to growth; (iii) the adsorbates enhance the growth rate and the adsorption and desorption rates are mutually proportional, i.e. $D \propto C$, in particular $D = \dfrac{C(1-\alpha)(1-\gamma+\gamma\alpha)}{\alpha(1+\gamma\alpha)}$.
Substituting condition (2) in to (3) implies that the PDE model (2) supports a multiplicity of spatially uniform equilibria, i.e. real solutions (η^*, θ^*) of the algebraic system composed of the two reaction terms. In particular, condition (2) ensures that: (i) the parameter C has no role in deciding the number and the numerical value of spatially uniform equilibria; (ii) for a specific choice of the other parameter values, it is easy to see that the number of spatially uniform equilibria (η^*, θ^*) changes by varying the parameter B (see [21]); (iii) in any case, $P_e = (\eta_e, \theta_e) = (0, \alpha)$ is a spatially independent equilibrium for any choice of all parameter values.
Since P_e is characterised by $\eta_e = 0$, it corresponds to a flat electrode surface, from which corrugation and morphology can develop. For this reason, the related stability properties and possible destabilization mechanisms are particularly relevant from the physical point of view.

Theoretical as well as numerical investigations have systematically corroborated the extreme flexibility of the nonlinear reaction diffusion system (2)-(3) in accounting for the great variety of spatio-temporal patterns found in the experimental electrochemical literature. It is worth recalling here a selection of the most representative achievements in this respect.

In [21], the problem of spatial pattern formation has been considered by focusing on the diffusion-driven or Turing instability mechanism: by using the classical methods of linear stability, conditions for the onset of Turing instability have been derived and a region in the parameter space has been determined, where spatially inhomogeneous solutions with some structure called *Turing patterns* are expected. In [21], the occurrence of a supercritical Hopf bifurcation for the local kinetics of the system has also been proved. This feature has two main dynamical implications. (a) Complex spatio-temporal behaviour can occur for the PDE system (2)-(3) when the choice of parameters corresponds to an oscillatory regime. This result can be explained with the capability of our system to support spiral wave behaviour as well as an interesting mechanism of spiral break up as discussed in [22, 46]. (b) The intriguing interplay between Hopf and Turing instability has been recognised to be responsible for the arising of a rich class of spatio-temporal patterns in the model in the neighbourhood of a codimension-two Turing-Hopf (TH) bifurcation point. In particular, it is worth noting that, as a result of the specific choice of the parameter values, two kinds of TH instabilities are possible for the homogeneous periodic solution: weak or strong TH. Weak instabilities are characterised by dominant inhomogeneous steady patterns superimposed to slightly time-periodic oscillations with the same frequency of the limit cycle. Strong instabilities instead imply the intermittent switching between the spatial inhomogeneous pattern and its complementary one.

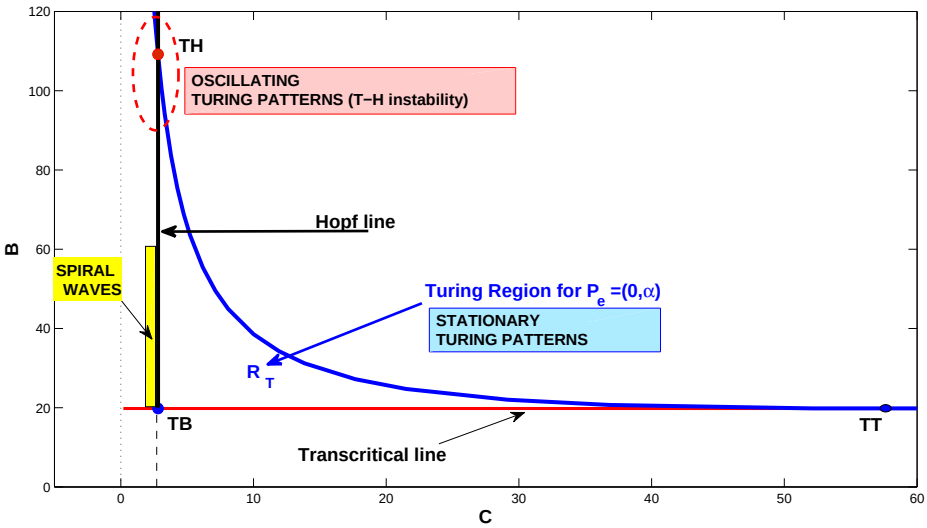

Figure 1. Bifurcation diagram in the parameter space (C, B) for $d = 20$. The values for the other parameters are: $\alpha = 0.5$; $\gamma = 0.2$; $k_2 = 2.5$; $k_3 = 1.5$; $A_1 = 10$. For this choice of the parameter values, the codimension-two bifurcation points TH and TB have coordinates $(C_{TH}, B_{TH}) = (2.8061, 109.13)$, $(C_{TB}, B_{TB}) = (2.8061, 19.7979)$. R_T is the Turing region where conditions for the Turing spatial pattern formation are satisfied.

2.1. *Bifurcation diagram*

In this subsection, we briefly summarise the bifurcation analysis detailed in the above cited papers in order to pinpoint more clearly the variety of morphochemical pattern types that can be generated by changing the values of only two key parameters, that is the parameters B and C in (3). It is these two parameters that we will seek to identify later in the paper in order to solve the related *inverse problem* and thus describe different experimental patterns. Following the analysis in [21], when all the other parameters in (2)-(3) are fixed to $d = 20$, $\alpha = 0.5$, $\gamma = 0.2$, $k_2 = 2.5$, $k_3 = 1.5$, $A_1 = 10$, the bifurcation diagram in Figure 1 can be obtained. It is worth noting that the values of A_2 and ρ do not affect the geometrical boundaries of the bifurcation diagram (see [21]). The diagram depicted in Figure 1 summarises qualitatively the variety of solutions present in the electrodeposition model, that is stationary and oscillating Turing patterns as well as spiral waves (as proved in [22]).

Linear stability analysis straightforwardly shows that there are two specific bifurcation pathways by which, in presence of diffusion, the spatially homogeneous and physically sound equilibrium $P_e = (0, \alpha)$ can lose the stability it exhibits in the absence of diffusion. One is the *transcritical bifurcation*, where the attracting equilibrium P_e loses its stability because it exchanges its stability properties with those of another equilibrium. If $J_e = J(\eta_e, \theta_e)$ is the Jacobian of the reaction part evaluated at the equilibrium P_e, at the bifurcation value, P_e becomes non-hyperbolic since one real eigenvalue of J_e vanishes. Hence, the transcritical bifurcation can be detected by requiring $\delta_e = \det(J(\eta_e, \theta_e)) = 0$. The other bifurcation mode involved is the *Hopf bifurcation*, where the attracting equilibrium P_e loses its stability because a pair of complex conjugate eigenvalues of J_e crosses the imaginary axis. The Hopf bifurcation can then be detected by requiring $\tau_e = \mathrm{tr}(J(\eta_e, \theta_e)) = 0$ and $\delta_e > 0$.

Figure 1 shows the corresponding bifurcation lines in the parameter space (C, B) for the above choice of the other parameter values: the vertical and horizontal lines are the Hopf and the transcritical lines, respectively. The regions on the right-hand side of the Hopf line and above

the transcritical line are characterized by $\tau_e < 0$ and $\delta_e > 0$, so that, in the spatially uniform case, the homogeneous equilibrium P_e is unconditionally stable. For parameter choices below the transcritical bifurcation line, $\delta_e < 0$ holds, so that P_e can be destabilized by small homogeneous perturbations and the system trajectories tend toward a different stable steady state (see also [43] for a detailed discussion on this point). Moreover, in the region on the left of the Hopf line and above the transcritical one, P_e is unstable and we expect homogeneous oscillations due to the presence of a stable limit cycle, caused by a supercritical Hopf bifurcation.

When diffusion mechanisms are considered, P_e can destabilise in the parameter region called R_T in Figure 1 where conditions for the Turing instability are satisfied: the formation of stationary spatial patterns is hence expected because of the interaction between the nonlinear reaction terms and the diffusion process. The specific typologies of Turing patterns and hence their spatial structure have been found solving the *direct problem* by means of several numerical simulations performed by sampling the R_T region with several values of the parameter couples (C, B), as reported in [21]. In Figure 1 the intersections between the two bifurcation lines is a point called TB, while their intersection points with the Turing region are called TH (Turing-Hopf) and TT (Turing-Transcritical), respectively. For the choice of the parameter values reported in the figure caption, the codimension-two bifurcation points TH and TB have coordinates $(C_{TH}, B_{TH}) = (2.8061, 109.13)$, $(C_{TB}, B_{TB}) = (2.8061, 19.7979)$. Figure 1 shows the Turing region R_T in the parameter space (C, B) corresponding to the diffusion parameter $d = 20$; it is worth noting that the size of the Turing region R_T increases for larger values of d. Recently, the results concerning Turing pattern formation for the morphochemical model have been extended in [44] to the case of the RD-PDE system defined on a sphere, and in [45] to account for cross-diffusion terms.

3. Identification Problems

In this paper we look for a *quantitative validation* of the mathematical model (2)-(3) based on parameter identification for a comprehensive set of experimental morphochemical maps covering the key patterns supported by it. As detailed in the papers cited above, during electrodeposition experiments it is possible to collect a range of different types of images, that pinpoint peculiar geometric and compositional aspects, that can be straightfowardly and quantitatively related to the morphology profile $h(x, y, t)$ in (1) and to the chemical distributions $\theta(x, y, t)$. Examples of *qualitative comparisons* between experiments and simulations of our model have been provided in [6] for a selection of OM (Optical Microscopy) and SEM (Scanning Electron Microscopy) images of structured patterns present in the literature (including target and spiral waves) and in the paper [7] for soft-X ray fluorescence maps that can be regarded as unstructured patterns.

It is worth noting that in many cases the experimental morphological and compositional distributions resulting from an electrochemical process represent the final configuration of a non-stationary process that has been stopped after a certain time. With limited loss of generality, in this paper we focus on a selection of experimental *structured* maps that can be considered as *stationary electrodeposits*: this implies that $\lim_{t\to\infty} \eta = \bar{\eta}$ and $\lim_{t\to\infty} \theta = \bar{\theta}$ where $\bar{\eta}, \bar{\theta}$ are time-independent. Hence, of course, $h(t) = \bar{\eta} \cdot t$, i.e. $h(t)$ does not change its shape as time lapses. The methodological reason of this choice is that we shall compare experimental data with stationary Turing patterns that are steady state solutions of the RD-PDE model (2)-(3). In this sense we are dealing with an *inverse problem* that we formulate as a nonlinear fitting problem for parameter estimation where the PDE model is the given constraint for the optimization problem. Hence, as a side result of parameter estimation, we shall introduce a mathematical tool yielding quantitative comparisons between experimental maps and simulations.

In view of achieving these goals, we shall consider our parameter identification problem for values in the Turing region R_T. In this initial study we consider only the case where we have a data map M^* corresponding to the chemical distribution θ. Hence, to express the above concept of *comparison* formally we formulate the following *identification problem.*

Parameter Identification Problem (PIP):
Given an experimental map $M^* \in \mathbb{R}^{n\times m}$, the time integration interval $[0,T]$ and the initial conditions $(\eta_0(x,y),\theta_0(x,y))$ in (4),
FIND a *suitable* parameter set $p^* \in \mathbb{R}^r$ for the model (2) such that $\theta(x,y,T) \approx M^*$, where θ is the solution of the RD-PDE system (2)-(3)-(4).

We take the standard approach of fitting the model to the data in a least squares sense, which is the approach used in many of the studies cited in the Introduction (see also the books [47] and [48]). Hence we formulate the *PIP problem* as follows:

FIND the parameters $p^* \in \mathbb{R}^r$ such that

$$J(p^*) = \min_p J(p),$$

with

$$J(p) = \frac{1}{2}\int_\Omega w(x,y)(\theta(x,y,T) - M^*)^2 dx\, dy, \tag{5}$$

where $w(x,y) > 0$ is a suitable weighting function and the solution $\theta \equiv \theta(p)$ of the RD-PDE system (2)-(3)-(4) at the final time T depends on the parameters p.

In this work, we particularly wish to associate the experimental maps to different parts of the (C,B)-bifurcation diagram associated to the RD model reported in Figure 1. Hence, we concentrate on the estimation of the parameters B and C, assuming that all other parameters in the model are fixed. In fact, as discussed above, in [21, 22] several numerical simulations were performed varying mainly B and C, that are also the more meaningful parameters from the electrochemical point of view. In some cases, the role of A_2 and ρ on pattern formation has been shown in [21, 44]. In this paper the main aim is to address in quantitative way the comparison with true experimental data. For this reason here we start to solve the inverse problem as a PIP in the simplest meaningful case, that is by considering only two constant parameters.

The case of non-constant parameters, for example when B and C are space and/or time dependent functions is also interesting for the electrodeposition model. This would be a harder problem and here we present just a first step in this direction. Current research is devoted to the case of variable parameters, that would imply also new analytical studies for the pattern formation problem.

Hence, the PIP in (5) can be expressed as follows:

FIND $(C^*, B^*) \in \mathbb{R}^2$ such that

$$J(C^*, B^*) = \min_{C,B} J(C,B)$$

where

$$J(C,B) = \frac{1}{2}\int_{\Omega} w(x,y)(\theta(x,y,T) - M^*)^2 dx\, dy \tag{6}$$

where $w(x,y) > 0$ is a suitable weighting function and θ is the solution of the RD-PDE system (2)-(3)-(4) at the final time T.

To solve (6), we follow the well-known *discretize-then-optimize* approach. Hence in the next section we consider the discrete form of this problem.

4. Discrete identification problem

The PDE system (2)-(3)-(4) is solved numerically on a spatial meshgrid $(x_i, y_j), i = 1,\ldots,n$, $j = 1,\ldots,m$ on $\Omega \subset \mathbb{R}^2$, as described in Appendix. We write the numerical solutions at discrete times $t_k = kh_t$, where h_t is the model time step, as $\eta_{ij}^k \approx \eta(x_i, y_j, t_k), \theta_{ij}^k \approx \theta(x_i, y_j, t_k)$. For the purpose of expressing the identification problem it is convenient to consider the two dimensional spatial fields mapped on to a vector. We indicate with the vector $\hat{\eta}^k \in \mathbb{R}^{nm\times 1}$ and $\hat{\theta}^k \in \mathbb{R}^{nm\times 1}$ these numerical solutions at time t_k.

We introduce the notation $\hat{M}^* \in \mathbb{R}^{nm\times 1}$ to indicate the 2-dimensional experimental map M^* mapped to a vector. Then the PIP discrete formulation is:

PIP

Given an experimental map $\hat{M}^* \in \mathbb{R}^{nm\times 1}$, initial conditions $\hat{\eta}_0 \in \mathbb{R}^{nm\times 1}, \hat{\theta}_0 \in \mathbb{R}^{nm\times 1}$ and the final time of integration $T > 0$
FIND the parameters $p^* = (C^*, B^*)$ that minimize the functional

$$J(C,B) = ||\hat{\theta}_T(C,B) - \hat{M}^*||_W^2, \tag{7}$$

subject to the discrete model

$$[\hat{\eta}_T, \hat{\theta}_T] = \mathcal{S}_T(\hat{\eta}_0, \hat{\theta}_0, C, B), \tag{8}$$

where $\mathcal{S}_T$ indicates the solution operator (numerical method) yielding the discrete version of the RD-PDE system (2) from time zero to time T. In (7) $||x||_W^2 = x^T W x$ and $W \in \mathbb{R}^{nm\times nm}$ is a weighting matrix. The choice of this matrix is discussed in section 4.2.

The initial conditions in (8) are fixed and are taken to be a perturbation of the equilibrium solution, of the form

$$\hat{\eta}_0 = \hat{\eta}_e + c_e X_\eta, \tag{9}$$

$$\hat{\theta}_0 = \hat{\theta}_e + c_e X_\theta, \tag{10}$$

where $\hat{\eta}_e$, $\hat{\theta}_e$ are given equilibrium values, X_η and X_θ are perturbation vectors and c_e is a scalar parameter. Such initial conditions guarantee the generation of patterns in the Turing region when $(\hat{\eta}_e, \hat{\theta}_e) \equiv P_e = (0, \alpha)$, that is the spatially homogeneous solution of the electrodeposition model discussed in Section 2.1. We note that, for the reasons expounded in Section 3, the final time T must

be specified *a priori*. Since we assume that the data map corresponds to a steady-state solution then this choice should not be too problematic, as it is sufficient to specify a final time that is long enough for the PDE steady state to be reached. We will discard possible optimal solutions that are not steady state PDE solutions. This will be done by an *a posteriori* check on the stabilization dynamics of the space mean value

$$\langle \theta(t) \rangle = |\Omega|^{-1} \int_{\Omega} \theta(x, y, t) dx\, dy \tag{11}$$

and on the increment between the times t_{n+1} and t_n, i.e. $\|\hat{\theta}^{n+1} - \hat{\theta}^n\|_2 \leqslant tol$ (see, for example, section 6.1).

4.1. *Solution procedure*

As discussed in the previous Section, Turing instability in reaction-diffusion systems means that in the model parameter space there exists a region where the PDE solutions exhibit some kind of pattern structure, that typically is found by numerical simulations.

For the DIB model, we refer to the Turing region R_T shown Figure 1. The Turing analytical study implies that in R_T we can have subregions that correspond to classes of solutions, that is labyrinths, spots, holes, etc and we do not know *a priori* whether these zones are empty or where they are located.

On the other hand, in the inverse problem for the given target pattern M^*, we know by visual inspection that it belongs to one of these classes. Therefore, our PIP (7)-(8) is indeed a two-step inverse problem because we want to identify:
i) first of all, the "position" in the parameter space of the right "given" pattern class;
ii) then the unique or an optimal solution in this class/ subregion.

In this paper, our idea is to consider appropriate approaches to deal separately with the above points (i) and (ii). To tackle the point (i), we propose a (two-norm) cost function (7) without regularization such that its lowest values can identify numerically the subregion (connected or not) of the Turing space, say S_T, where qualitatively similar solutions are present. A plot of this cost function over a sample of values of the parameters B and C will allow us to identify this subregion, as well as an approximate location (C_0, B_0) of the possible minimum value(s). Hence, this will be a numerical tool to locate the subregion of parameters corresponding to the class of patterns similar to the target one. We note that the position of these subregions will depend on the chosen value of the parameter A_2. In future work it would be interesting to also optimize for this parameter. For this study we fix the value of A_2 so as to ensure that the cost function has well-defined subregions.

To solve the above point (ii), we test the addition of a classical Tikhonov regularization term (see [50, Chap. 5], [40]) to the cost function (7), centered on values (C_r, B_r) in the subregion S_T found by PIP(i). Thus the original cost function (7) is replaced by the function

$$J(C, B) = ||\hat{\theta}_T(C, B) - \hat{M}^*||_W^2 + \gamma_B ||B - B_r||_2^2 + \gamma_C ||C - C_r||_2^2, \tag{12}$$

where γ_B, γ_C are weighting parameters to be chosen.

This regularized cost function is then optimized using an iterative minimization algorithm, starting from a suitable starting guess, to identify a well-posed optimal solution of the PIP in the pattern class identified by the subregion S_T. In the absence of any other information, the values (C_r, B_r) are the current best estimate of the solution and so these values are used as the starting

guess. However, in some of the discussion below we also report on experiments where the starting guess was taken to be further away. Several methods for choosing the appropriate regularization parameters, such as the L-curve or the discrepancy principle, have been developed for linear least squares problems with a single regularization parameter [50]. For a nonlinear least-squares problem with multiple parameters, such as the one studied here, the classical methods cannot be applied exactly. There has been recent work on how to extend the standard methods to these cases (e.g. [51], [52], [53]), but detailed application of these is beyond the scope of this study. In the numerical results we choose the parameters γ_B and γ_C in (12) to give sufficient weighting with respect to the data term in the cost function.

In solving PIP(ii), optimization of the cost function is performed using the Polack-Ribiere flavour of a conjugate gradient method [54, Sec 5.2]. This is a gradient-based method that requires the gradient of the objective function with respect to the parameters on each iteration. For many large-scale optimization problems the gradient information is obtained from the adjoint equations. By introducing Lagrange multipliers and forming the discrete Euler-Lagrange equations it can be shown that the gradient of the objective function with respect to its parameters can be found efficiently from just one simulation of the discrete adjoint equation (see, for example, [55]). When using the discretize-then-optimize approach we need the gradient of the discrete cost function, which requires the adjoint of the discrete nonlinear model. In practice this can easily be derived directly from the source code of the nonlinear model, in a process known as automatic differentiation (e.g. [56]). This is the approach that we follow here.

The minimization is terminated when the norm of the gradient vector relative to the initial norm falls below a specified tolerance. We note that, in common with other gradient based methods that are often used in inverse problems, the conjugate gradient method is only guaranteed to converge to a local minimum. The speed and accuracy of convergence of this method is bounded by the condition number of the Hessian of the problem [57]. The two-step procedure used here enables a local minimum point in the correct zone to be found. It is worth noting that in applications involving experimental data, solving PIP(i) is necessary, in order to locate regions of the parameter space corresponding to the pattern class to which the target pattern belongs, while solving PIP(ii) and removing potential ill-posedness are required only to refine the matching between the parameter values and the target pattern. In fact, in a physical investigation sometimes it can be enough to identify a range of parameters generating any pattern in the given target class, or to regularize around a set of parameter values having a specific physico-chemical meaning.

Before presenting numerical results for simulated and true data, we examine in more detail the choice of the weighting matrix W in (7).

4.2. *Choice of weighting matrix*

The weighting matrix W serves to give importance to different parts of the data map in the optimization problem, allowing the model to fit some parts better than others. In the absence of any other information about the map then it is natural to choose W as the identity matrix. However other choices may be more appropriate if more information is available. If the measurements at different parts of the map are known to have different variances, then W may be chosen as a diagonal matrix containing the inverses of these variances. In this case the optimization problem can be interpreted statistically as a maximum likelihood problem [49, Sec. 3.2]. This approach may be extended if correlations between errors in different parts of the data map are known, by including these correlations in the off-diagonal elements of W.

In the experiments below we investigate the use of a weighting matrix based on the data values themselves, that is we choose W as a diagonal matrix with entries dependent on the values

of the map $\hat{M}^*$. In particular, in Section 6.4, we use this technique to identify parameters for a data map consisting of an almost homogeneous field with scattered holes. By giving more importance to the pixels of the map where the holes are present (lower absolute values), we aim to emphasise the fit to the patterns evident in the data.

5. Numerical results: simulated data

In this section, we present some numerical results obtained by solving the parameter identification problem (7)-(8) for the two parameters B and C. At each step of the optimization algorithm, the discrete model in (8) has been obtained by solving the PDE reaction-diffusion system (2)-(3) by means of the ADI-ECDF method described in the Appendix.

We decide to present our numerical simulations for a comprehensive selection of data maps M^*, to show that we are able to associate each class of data to an appropriate subregion of the bifurcation diagram in Figure 1. This will be the main result of our paper, because
(i) by solving the inverse problem we are able to recover the rich scenario of solutions provided by the model presented in [6, 21, 44];
(ii) on the other hand this approach gives a quantitative association between data and numerical simulations and so yields a stronger physical validation of our PDE morphochemical model;
(iii) this association between typology of experimental data with a theoretical bifurcation diagram can in principle be useful to control an electrodeposition process by tuning the parameters B and C that correspond to specific values of the process parameters that can be straightforwardly manipulated by applying appropriate electrochemical control and/or by selecting a suitable bath chemistry.

In this section, we fix all the parameters of the PDE in (2)-(3), except B and C, as described in the caption of Figure 1, including also the values of d, c_e, ρ. We choose the values of the parameter A_2 and of the final time T according to the typology of data, as discussed below; we choose the scaling factor $\rho = 1$ and the domain of integration fixed to be $\Omega = [0, 50] \times [0, 36]$.

In each simulation we normalize the data map M^*, because we are interested in the shape of the experimental pattern independently from its numerical values, so the comparisons will be made with the model solution $\theta(x, y, T)$ normalized between 0 and 1 which, with a slight abuse of notation, we continue to refer to as θ.

Hence, we can study and represent the cost function (7) without regularization terms by contour plots in a subdomain of the bifurcation diagram, say $\mathcal{R}= [C_1, C_2] \times [B_1, B_2]$. We will study Turing patterns that are labyrinths, reversed spots (holes), reversed spots and worms, mixed spots and stripes (as described in [21, 44]), that is solutions inhomogeneous in space with a well-identified texture. Based on the numerical results in [21], we decide first of all to work on data that are generated synthetically, that is M^* is indeed obtained by solving numerically the *direct problem* corresponding to known parameter values $(C^*, B^*) \in R_T$ in the Turing region.

Hence, first of all, in the next subsection we study the corresponding cost function (7) in the Turing zone, where of course $J(C, B)$ will have an absolute minimum, but in addition its form around this minimum will segment the bifurcation diagram into subregions corresponding to different patterns. Since we know [21] that in the Turing-Hopf zone solutions oscillating both in space and time are present, exhibiting different amplitudes and frequencies depending from the parameter values, we decide to investigate the PIP problem in this zone in future research, devoted to the analysis of experimental maps that are non stationary and with a non well-identified texture in space that cannot straightforwardly be classified according to the pattern categories listed in subsection 5.2. (see [7] for qualitative comparisons in this case).

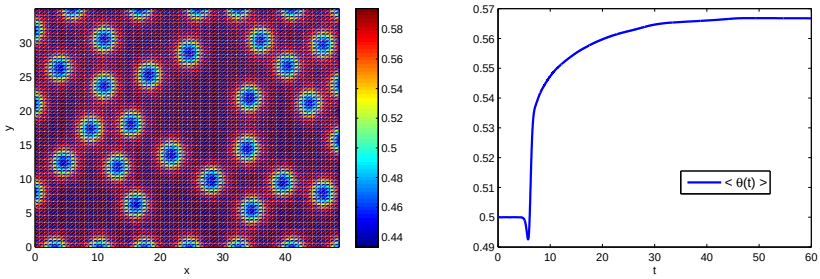

(a) Reversed spots/Holes: $A_2 = 1$, $(C, B) = (3, 30)$, $T = 60$

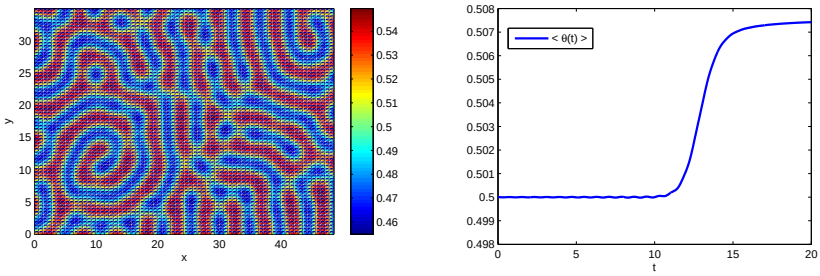

(b) Labyrinth:$A_2 = 1$, $(C, B) = (3, 66)$, $T = 20$

Figure 2. Simulated data. On the left: Turing patterns for the surface chemistry $\theta(x, y, T)$ in the electrodeposition model (2) at the final time T of integration. On the right: time behaviour of the corresponding mean space integral in (11).

5.1. *Parameter optimization*

As initial guess for the PDE model we consider a perturbation of the homogeneous steady state (9)-(10), where X_η and X_θ are random matrices of fixed size $N_x \times N_y$. Here, $c_e = 1e$-5 is fixed. In the Turing zone R_T we consider the cost function for two types of solutions, labyrinths and reversed spots/ holes, corresponding to the *true* parameters $(C_t, B_t) = (3, 66)$ and $(3, 30)$ respectively. For the labyrinths and for the reversed spots/holes we fix $A_2 = 1$. Since Turing patterns are stationary solutions obtained for long time, we fix a sufficiently large integration time T. For the labyrinths we choose $T = 20$, while for the holes we choose $T = 60$. We solve the PDE model by means of the ADI-ECDF method (see the Appendix for more details) of order $p = 2$ and using $h_t = 0.01$ as timestep. The meshpoints in space are $N_x = N_y = 70$ for these simulations. We note that by changing the meshgrid size we can obtain slightly different patterns but all belonging to the same class (see discussion below). (In fact, the variation of N_x, N_y implies changing both the discretized initial conditions and the size of the ODE system corresponding to the space semidiscretization, see Appendix). The simulated patterns at the end of the integration are shown in Figure 2 (a), (b) left plots, for the holes and the labyrinth, respectively. In the same figure, right plots, we show the time dynamics of an approximation of the mean space integral $\langle \theta(t) \rangle$ in (11) : it is evident in both cases (a) and (b) that a constant value is obtained for final times, as an indicator that a stationary pattern has been attained at time T.

The corresponding contour plots of the cost function $J(C, B)$ in (7) are shown in Figure 3, with that for the reversed spots/holes in panel (a) and for the labyrinth in panel (b). In Figure 3 we show also the boundary of the Turing region by white curves. Hence, we can solve the PIP(i) identifying the subregions S_T of patterns with similar structure as follows. For the case of the holes, we find for values of B between 25 and 35, one smaller area S_T of low function values around the minimum for C up to around 4. Instead, for the labyrinth we find S_T as a long valley around the true minimum

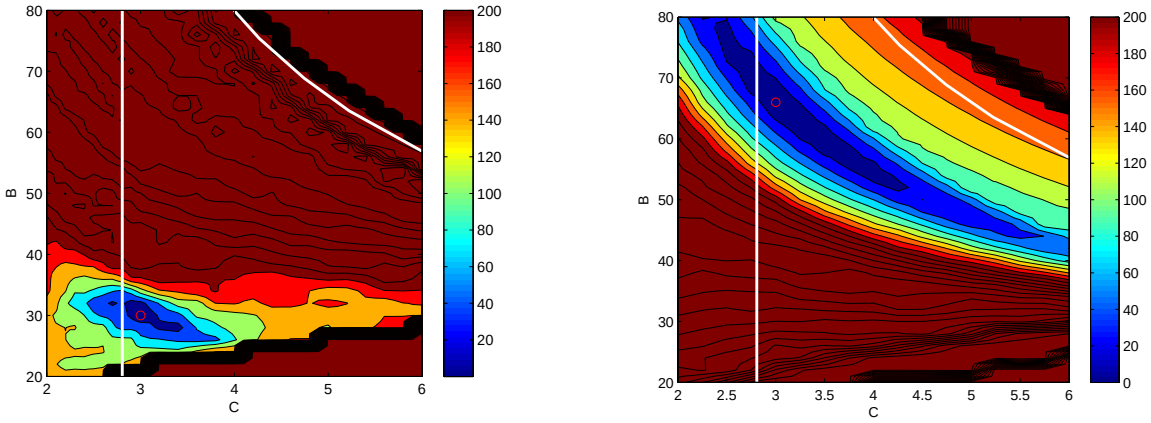

(a) Reversed spots: $(C_{tr}, B_{tr}) = (3, 30)$, $T = 60$

(b) Labyrinth: $(C_{tr}, B_{tr}) = (3, 66)$, $T = 20$

Figure 3. PIP cost functions $J(C, B)$ (unweighted $W = I_d$) when $M*$ in (6) corresponds to simulated data in Figure 2 (a) and (b), respectively

(C_{tr}, B_{tr}), indicating a large region of parameters yielding labyrinth-like structures.

In both plots we identify the same region of high, flat values of the cost function in the lower right part of the pictures. Numerical simulations show that in that region the holes disappear and a spatially homogeneous solution appears whose value is $\theta_{ss} = 0.5969$. This is different from the equilibrium value of θ_e and corresponds to another steady-state equilibrium of the model (see [43] and Figure 1 in [21]). On the other hand, the similar flat regions present in the upper right part of the figures correspond to the homogeneous steady state $\theta_e = 0.5$ in P_e that we are considering.

To show the convergence properties of the optimization algorithm presented in the previous section, we solve the PIP(i) and PIP(ii) steps in the case of the simulated labyrinth with noisy data. The synthetic observation is generated from the model field at time T=20, with unbiased, random, Gaussian noise added. In practice we expect the standard deviation of the noise on the experimental data to be of the order of a few percent [58], [59]. Here, for the synthetic normalized data, we present results where the standard deviation of the noise is taken to be 0.1, representing 10% of the maximum value of the field. Similar results have also been obtained with a higher noise level of 20% (not shown). In Figure 4 top left plot we show the cost function for the noisy data. A comparison with Figure 3(b) shows a very similar pattern to the perfect observation case, with one zone of low cost function values.

We choose as initial guess $(C_0, B_0) = (2.9, 80)$, a point far from the minimum value, and we show the corresponding numerical solution of the model used as first guess pattern in Figure 4, upper right subplot. The obtained convergence history in shown in the lower left subplot of Figure 4, where the tolerance on the relative gradient is set to $tol = 1e\text{-}5$ and maxiter= 20.

The optimized pattern attained by the descent algorithm is shown in Figure 4, lower middle subplot. We find the following relative errors with respect to the true solution:
for the patterns: $\text{relerr}_0 = 0.3225$, $\text{relerr}* = 0.1955$ are the relative errors in the Frobenius norm of the first guess $\theta_0(x, y, T)$ and the optimal map $\theta^*(x, y, T)$ with respect to the simulated noisy one (shown in Figure 4 upper middle subplot), respectively;
for the parameters: $relerr_B = \frac{|B*-B_{tr}|}{|B_{tr}|} = 0.008$, $relerr_C = \frac{|C*-C_{tr}|}{|C_{tr}|} = 0.0175$. For this case the condition number of the Hessian is approximately $7.4e4$. In further experiments with a Tikhonov regularization of the form (12), with values $(C_0, B_0) = (5, 60)$, the final values obtained are very

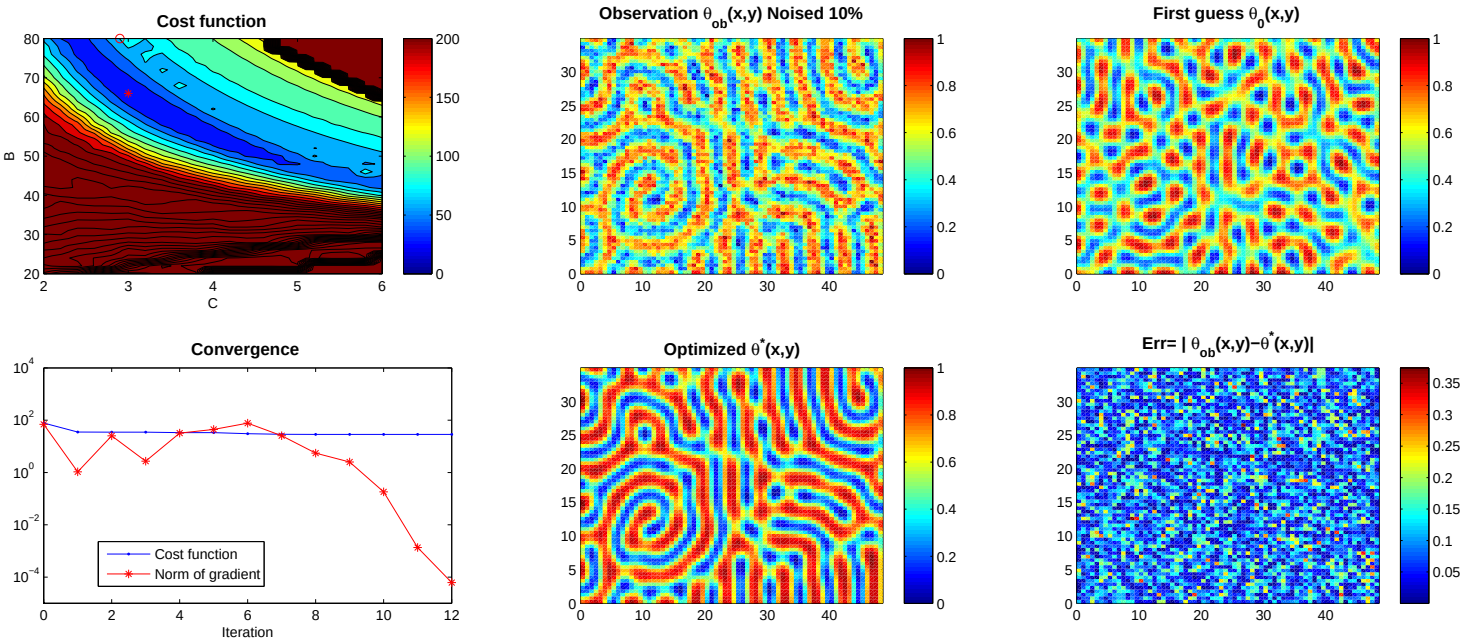

Figure 4. Simulated labyrinth for $(C_{tr}, B_{tr}) = (3, 66)$ with 10% noise: : optimization results. The upper panels show the cost function (left), simulated observation (middle) and first guess pattern $\theta_0(x, y, T)$ for $(C_0, B_0) = (2.9, 80)$ (right) The lower panels show the convergence of the cost function and gradient norm (left), the optimal pattern solution $\theta^*(x, y, T)$ after 12 iterations (middle) and the absolute error map (right). The relative errors in the Frobenius norm of the first guess $\theta_0(x, y, T)$ and the optimal map $\theta^*(x, y, T)$ wrt the simulated one are $\text{relerr}_0 = 0.3225$, $\text{relerr}^* = 0.1995$, respectively, and the maximum absolute error in the optimized solution is maxerr$= 0.3744$. The relative errors on the parameters is given by $\text{relerr}_B = 0.008$, $\text{relerr}_C = 0.0175$.

.

similar, with the relative error norm identical to 5 decimal places. Since the zone of minimum values is well-defined even with the noisy data, the algorithm is able to find a solution that is much better than the initial starting point, both in terms of error norm and the pattern produced.

5.2. *Segmentation of the Turing region*

Information collected from the above cost functions and from further simulations with parameters in the area $\mathcal{R}= [2, 6] \times [20, 80]$ of the bifurcation diagram in Figure 1 show interesting features. We synthesize these results in Figure 5, where we show a segmentation of the Turing region in significant parts. We identify six subregions, that we call R_0, $R_1 \ldots, R_5$ that are highlighted in Figure 5 with different colours. In each subregion we consider a selection of parameter values (C, B) to describe the different kinds of patterns present. In Figure 5, we report these choices of parameters by different symbols and we associate a small letter from a to m to each of them. Each letter identifies the corresponding (stationary) pattern shown on the right.

Hence, for decreasing values of B the $R_i, i = 0, \ldots, 5$ subregions are given by:
$\mathbf{R_0}$: is all the zone above the Turing boundary. Here the solutions tend to the homogeneous equilibrium equal to θ_e and Turing instability disappears.
$\mathbf{R_1}$ mixed-spots-stripes: is the interior zone of the Turing region near its boundary. Here the stationary solutions are mixed spot-stripes patterns. There is a predominance of spots near the

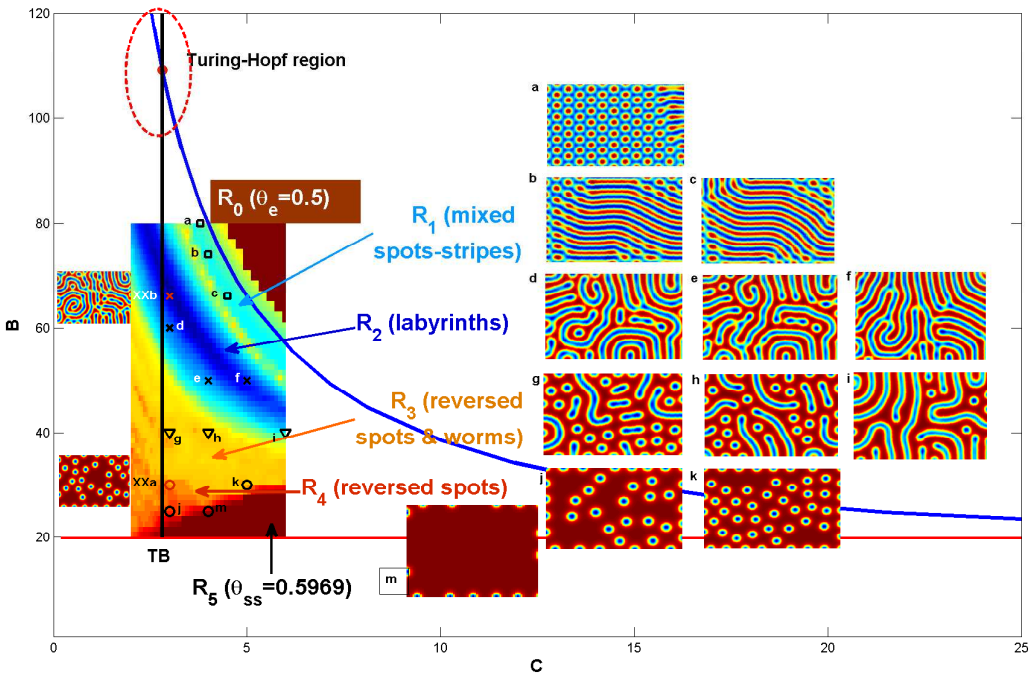

Figure 5. Segmentation of the Turing region: six subregions $R_0, R_1 \ldots, R_5$ from top to bottom are identified in the bifurcation diagram of Figure 1. In each subregion we report a selection of parameter couples (C, B), indicated by a symbol and a letter. Each letter from a to m identifies the corresponding (stationary) pattern shown on the right part of the figure. The parameter couples XX_a and XX_b (red cross and circle) and the (smaller) patterns reported on the left of the Hopf line are the simulated labyrinth and holes analyzed in Figure 2. For further details on the classification of the zones $R_i, i = 0, \ldots, 5$ see the main text.

boundary (see pattern a) and more stripes far from the boundary (see patterns b, c). We note that in [21] we find similar solutions for $B = 90, C = 3$, that is near the border with the Turing-Hopf region, in the "cuspidal" zone of the bifurcation diagram.

R_2 labyrinths: the blue zone is full of solutions similar to the simulated labyrinth reported in Figure 2b. Patterns d, e, f show labyrinths with different arrangements of their arms, that tend to be longer and better aligned for increasing values of C.

R_3 reversed spots & worms: the yellow zone is between the labyrinth and holes regions. This is like a transition zone where for decreasing values of B the labyrinths are flattened and the arms are fragmented in reversed spots and worms that are in fact holes of these particular shapes. The worms become longer and predominant for increasing values of C (patterns g, h, i).

R_4 reversed spots/holes: this zone was identified thanks to the cost function in Figure 3(a). The simulated pattern is reported in the small picture on the left of the Hopf line (bottom). These spots are indeed holes on a flat surface. The number of holes increases for increasing values of C (patterns j, k)

R_5: this region is just above the transcritical line. Here even if inside the Turing region, the stationary solution is not a Turing pattern, but the destabilization of the equilbrium θ_e leads to another spatially homogeneous equilibrium $\theta_{ss} \neq \theta_e$. For (C, B) values on the boundary shared with the R_4 zone we show the pattern m corresponding to an almost flat surface with few spots entering "from" the border.

In conclusion, in the Turing zone we find subregions where parameters can describe several types of structured data. Furthermore, these subregions are found to be contiguous and topologically

simply connected. In this section, we have shown that, by using the PIP cost function with synthetic data as a quantitative tool, we can classify the rich variety of solutions that the model can produce, splitting the bifurcation diagram into subregions corresponding to different types of solutions.

Remark 5.1. *It is worth noting that: (i) the segmentation has been obtained for $A_2 = 1$ and $N_x = N_y = 70$ meshpoints in all simulation snapshots; (ii) each pattern snapshot has been obtained for a final time T (value not reported) such that the steady state of the PDE model has been reached, in particular longer transient dynamics arises for parameter values towards the curved boundary of the Turing region, that is in R_1; (iii) for different values of N_x, N_y, that is the size of the discretization in* (8) *and hence the number of constraints in PIP, slightly different patterns could be obtained, in any case each one belongs to the same corresponding subregion $R_i, i = 0, \ldots, 5$; (iv) for increasing values of A_2 the scenario in the lower part of the Turing region changes, that is the regions R_3, R_4, R_5 disappear and the R_2 region of labyrinths of different shapes englobes them. A theoretical analysis on the role of the parameter A_2 deserves further studies; a qualitative discussion on this point was already given in [21].*

In the next section we demonstrate how we can use these results to inform the parameter identification problem PIP to deal with true experimental data maps.

6. True data

Thanks to the segmentation obtained for the Turing region in the bifurcation diagram of our model, we decide to solve the PIP problem for four different kinds of experimental maps from recent literature in electrochemistry that by visual inspection correspond to data patterns in the subregions R_1-mixed spots-stripes, R_2-labyrinths, R_3-reversed spots and worms, R_4-reversed spots. In particular, we extract them from the references indicated below and we assume that they exhibit stationary electrodeposit morphologies. As for the simulated data in the previous section, also here we normalize the data map M^* because we are interested in the shape of the experimental pattern independently from its numerical values, so the comparisons will be done with the solutions of the morphochemical model normalized between 0 and 1.

In all following examples, we calculate the PIP cost function in the Turing zone for ICs of the PDE model that are perturbations of the equilibrium P_e such that in (9)-(10) X_η, X_θ are the data normalized and then vectorized. We consider in all examples $c_e = 1e\text{-}5$ and the integration domain is now square given by $\Omega = [0, 50] \times [0, 50]$. If not otherwise stated, we fix the scaling parameter $\rho = 1$ and $A_2 = 1$. Each cost function will be calculated on a coarse grid of a subdomain $\mathcal{R} = [C_1, C_2] \times [B_1, B_2]$ of the Turing region. For this reason, its plot will indicate the parameter zones where patterns *more similar* to the data are present so suggesting where an initial guess for the optimization could be chosen.

In all simulations, we fix the following values for the numerical discretization of the electrodeposition PDE model (see Appendix): timestep $h_t = 0.01$, space meshsize $N_x = N_y = 100$ (corresponding to the pixel size of the given data image).

6.1. *R_1-mixed-spots-stripes*

In this example, the data map $M_1 \in R^{N \times N}$, $N = 100$ pixels is extracted by [6] (Supplementary Information, p.1, Ag/Sb alloy ref [3] therein). We report the data indicated as $\theta_{ob}(x, y) = M_1$ in Figure 7, upper right corner. As we have seen for the construction of the Turing zone segmentation,

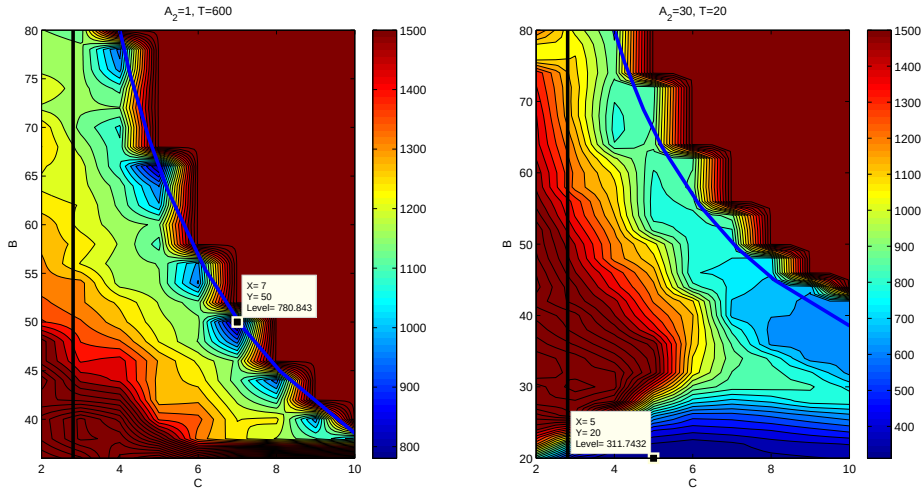

Figure 6. R_1-mixed-spots-stripes: Cost function for $A_2 = 1, T = 600$ on $\mathcal{R}= [2, 10] \times [35, 80]$ (left); cost function for $A_2 = 30, T = 20$ on $\mathcal{R}= [2, 10] \times [20, 80]$(right)

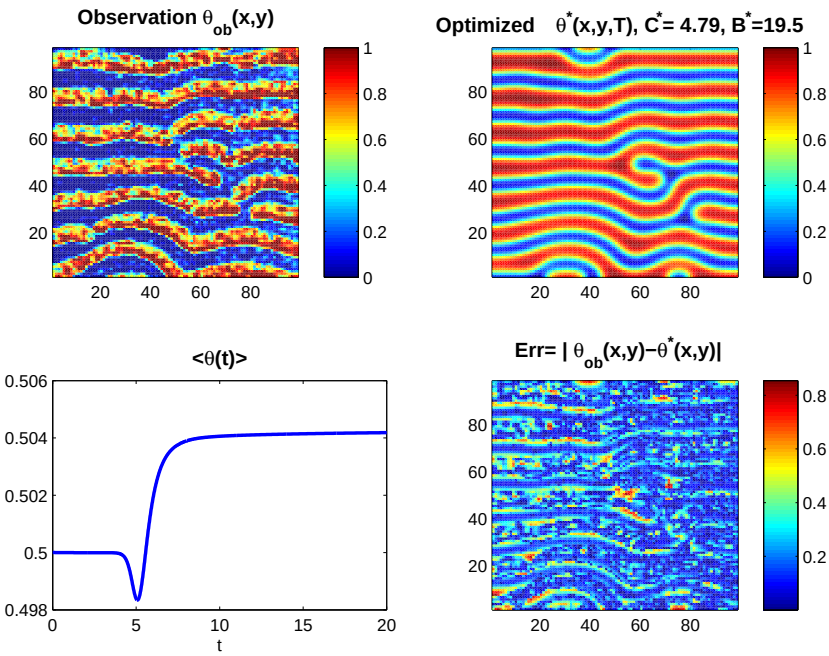

Figure 7. R_1-mixed-spots-stripes. Top line: true data map (left); simulated solution $\theta^*(x, y, T)$ for the minimum value $(C^*, B^*) = (4.7914, 19.5127)$ obtained by the optimization algorithm starting from $(C_0, B_0) = (5, 20)$ localized by the PIP cost function in Figure 6 (right). Bottom line: dynamics of the corresponding spatial mean $< \theta(t) >$(left); absolute error map wrt the data which maximum value is maxerr=0.8542.

mixed-spots-stripes can be obtained for long-time simulations of the electrodeposition model. Moreover, it is difficult to *stabilize* the pattern when the parameter values (C, B) are near the boundary of the Turing region. In this section, we show that this behaviour is reflected also for the true data. For this reason we fix the final time as $T = 600$. We solve the first step PIP(i) and then we calculate the PIP cost function (7) on a coarse grid on $\mathcal{R}= [2, 10]\times[35, 80]$ and we show in Figure 6, left panel,

that multiple local minima are present near the Turing boundary. For $20 \leqslant B \leqslant 35$, high values of the cost function are obtained, including a flat subzone where a spatially homogeneous solution different form θ_e is obtained. The *lowest* minimum here identified is $(C_{min}, B_{min}) = (7, 50)$, such that $J_{min} = 708.43$. Indeed, by performing the simulation of the model for this set of parameter we see that the dynamics is still in the transient and a minimum is attained because the solution is still near the initial condition of the PDE model, that is $\theta(x, y, T) \simeq \theta_0(x, y)$. On the other hand, if we look at the simulation for parameter values near (C_{min}, B_{min}), for example $(C, B) = (4.5, 65)$ where $J(C, B) = 1000.2$, we obtain stationary stripes but with very large errors with respect to the data.

In conclusion, we can say that PIP is ill-posed and ill-conditioned in this setting, with multiple disconnected zones of low cost function values. Hence, motivated by the remark on the role of A_2 highlighted at the end of the previous section, and also discussed in [21], we change the value of A_2 from one to 30. For this choice, we calculate the PIP cost function $J(C, B)$ on a coarse grid on $\mathcal{R}= [2, 10] \times [20, 80]$ and we report it in Figure 6, right panel.

We note that there are now two disctinct and clearly-defined zones of low cost function values. Here it is evident that there exists a minimum near $(C^*, B^*) = (5, 20)$ far from the Turing curved boundary but in the lower part of the bifurcation diagram, thus confirming Remark 5.1(iv). The corresponding pattern $\theta^*(x, y, T)$ generated using these parameter values results in a relative error in the Frobenius norm of relerr* $= 0.438$. If we solve PIP(ii) by using $(5, 20)$ as the first guess of the optimization algorithm without regularization, then the algorithm converges immediately to values of $(C^*, B^*) = (4.7914, 19.5127)$, with a small improvement in the solution. The corresponding pattern $\theta^*(x, y, T)$ is shown in Figure 7, upper right subplot. In Figure 7, lower left plot, the time dynamics of the space mean integral $\langle \theta^*(t) \rangle$ for the optimal solution shows that the stationary state is attained at $T = 20$. In Figure 7, lower right plot we show the spatial (absolute) error map $Err = |\theta_{ob}(x, y) - \theta^*(x, y, T)|$ which has a maximum value maxerr= 0.8542 (attained in very few pixels), while the corresponding relative error in the Frobenius norm is relerr* $= 0.435$. We note that this optimized solution actually lies below the transcritical line.

It is worth noting that, as already noticed in the previous section, this confirms that the parameter conditions to define the Turing region are necessary conditions. This means that patterns below the transcritical line can exist due to the diffusion-driven instability of another equilibrium of the DIB model different from $P_e = (0, 0.5)$. A discussion on this point is reported in[43].

For this case the problem is very well posed, with the condition number of the Hessian being of order 10. A Tikhonov regularization around the point $(5, 20)$ does not lead to any improvement. However, we note that if we start the minimization from the point $(8, 40)$, which lies in the other zone of low cost function values, then the iterates remain in that other zone and the algorithm converges to a local minimum of $(13.6249, 25.8221)$, with error norm 0.440. This is the case even with a modest Tikhonov regularization, for example using $\gamma_B = \gamma_C = 5$. Hence we see the advantage of the two-step PIP procedure used here, where first the correct zone S_T is identified and then the optimization is started from a point within that zone.

6.2. *R_2-labyrinths*

In this example, the data map $M_2 \in R^{N \times N}$, $N = 100$ pixels is extracted by [6] (Supplementary Information, p.2, entangled labyrinth Ag/Sb alloy ref [4] therein). Hence, in the PIP problem we have again $N_x = N_y = 100$. We report the data $\theta_{ob}(x, y) = M_2$ in Figure 8a, upper left subplot. We fix $A_2 = 30$ and $T = 20$. We solve the first step PIP(i) by calculating numerically the PIP cost function in $\mathcal{R}$=$[2, 10] \times [20, 70]$ on a rough meshgrid and we report it in Figure 8b, left subplot. The minimum zone S_T is located in the lower part of the Turing region. We decide to start the

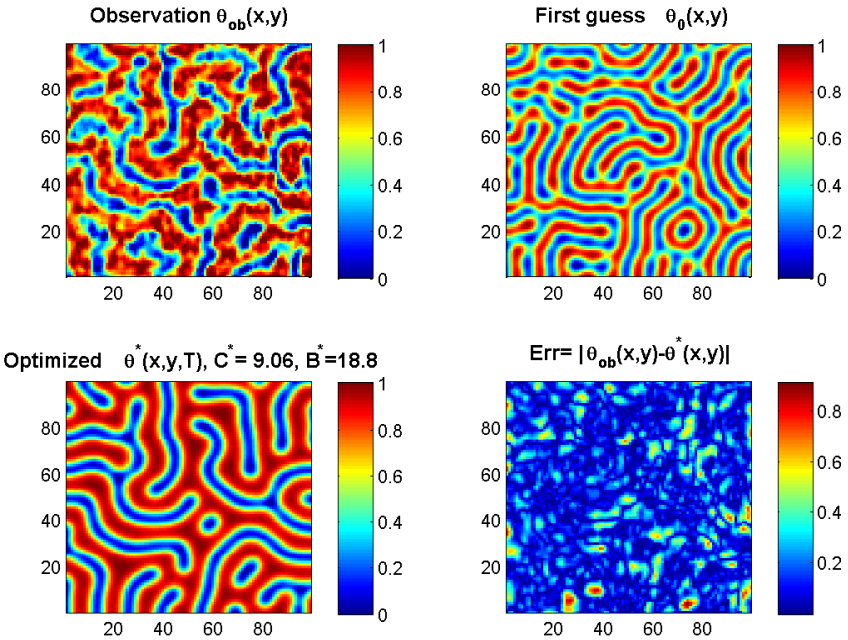

(a) Top line: true data map (left); first guess pattern $\theta_0(x, y, T)$ corresponding to $(C_0, B_0) = (3, 66)$(right). Bottom line: optimal pattern $\theta^*(x, y, T)$ obtained for $(C^*, B^*) = (9.0598, 18.8177)$(left); absolute error map Err (right) which maximum is maxerr= 0.9104, while the relative errors in Frobenius norm of the first guess and of the optimal pattern are relerr$_0$ = 0.6609, relerr* = 0.3108, respectively.

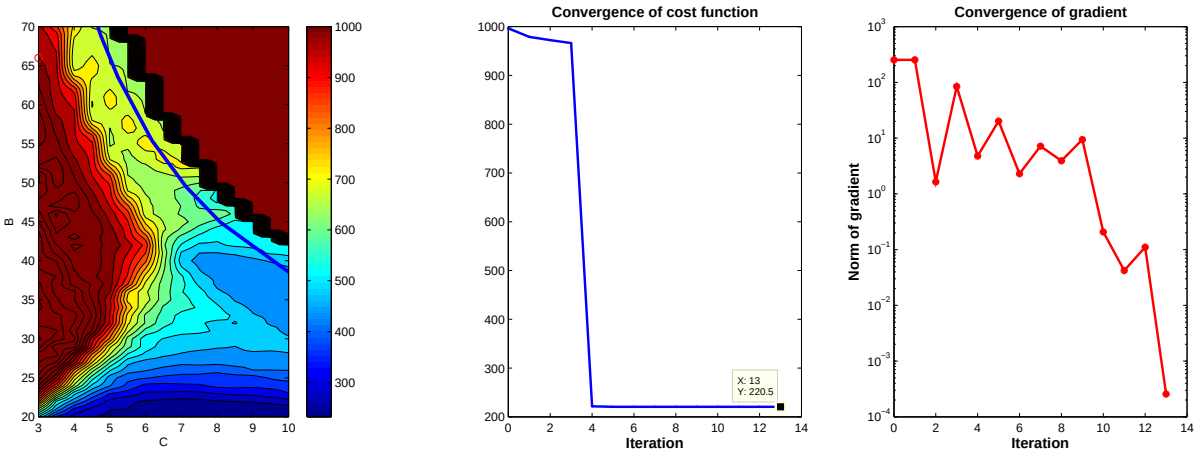

(b) From left to right: contours of cost function; convergence of the cost function; convergence of the norm of the gradient

Figure 8. R_2-Labyrinths

optimization algorithm from the parameter couple $(C_0, B_0) = (3, 66)$ far from the S_T identified but that for different A_2 and Ω yielded a labyrinthine-like structure (compare with Figure 2b). The first guess pattern θ_0 is shown in Figure 8a, upper right subplot. By applying the optimization algorithm, we find the optimal parameter set $(C^*, B^*) = (9.0598, 18.8177)$; the corresponding optimal Turing pattern $\theta^*(x, y, T)$ is shown in Figure 8a, lower left subplot. The absolute error map $Err = |\theta_{ob}(x, y) - \theta^*(x, y, T)|$ is reported in Figure 8a, lower right subplot. Its maximum value

is maxerr= 0.9104 attained in few spatial zones of the pattern. We calculate also the relative errors in Frobenius norm of the first guess $\theta_0(x, y, T)$ and of the optimal pattern $\theta^*(x, y, T)$ with respect to the data. They are given by relerr$_0$ = 0.6609 and relerr* = 0.3108, respectively, showing that a good improvement is obtained by using the optimization procedure.

In Figure 8b we show also the convergence history of the minimizing algorithm: in the middle subplot the behaviour of the PIP cost function $J(C, B)$ against the iterations and in the right subplot the corresponding convergence of the norm of the gradient. Here and in the next examples, we set tol = 1e-5 and max$_{iter}$ = 20 for the stopping criteria of the optimization algorithm. We see that for this case in 14 iterations the gradient norm does reduce by 5 orders of magnitude as required, while the value of the function converges to a value of just over 600. When trying to fit experimental data we do not expect the value of J to go to zero, as happened in the synthetic data case, since even at the exact minimum there will be a mismatch between the experimental data and the model prediction.

As for the case of the true data R_1, there are two zones of low cost function values in the parameter space. If we evaluate the approximate condition number of the Hessian at the starting point $(3, 66)$, we find it is quite is quite high, of order 10^5. Despite this, even without regularization we converge to a solution that gives a much lower relative error norm than the first guess. We note that, as for the data R_1, the optimized values lie below the transcritical line, indicating that we have converged to a solution that is the instability of a different equilibrium.

If we include a Tikhonov regularization around the point $(7, 21)$, then the behaviour depends heavily on the weighting given to the regularization terms. With $\gamma_B = \gamma_C = 0.01$ we converge to a slightly improved solution (in terms of the relative error norm), but in the parameter space below the transcritical line. However, for $\gamma_B = 0.001, \gamma_C = 0.1$ (chosen so both terms have a similar magnitude), then the algorithm converges to a local minimum in the other zone of low cost function values. However the patterns arising from these solutions do not resemble the labyrinth in the data. If the minimization is started from the point $(7, 21)$, then it converges quickly, with or without regularization, to values $(C^*, B^*) = (7.5460, 20.3527)$ and the relative error norm is given by relerr* = 0.3237.

6.3. *R_3- reversed spots & worms*

In this example, the data map $M_3 \in R^{N\times N}$, $N = 100$ pixels is extracted by [6] (Supplementary Information, p.2, spots & worms Ag/Sn alloy ref [41] therein). Hence, in the PIP problem we have again $N_x = N_y = 100$. We report the data $\theta_{ob}(x, y) = M_3$ in Figure 9a, upper left corner. We fix the values of $A_2 = 5$ and $T = 30$ as in Fig.6 of [21] (see also the discussion on the role of A_2 therein).

The PIP cost function on $\mathcal{R}$=$[2, 10] \times [20, 80]$ is reported in Figure 9b (left), where on a rough meshgrid the minimum is attained at $(C, B) = (8, 28)$ and $J(C, B) = 615.9517$. The optimization starting near this value from $(C_0, B_0) = (7, 25)$ attains the minimum at $(C^*, B^*) = (8.5096, 28.2614)$. The pattern corresponding to the first guess and the optimal pattern are shown in Figure 9a, upper right subplot and lower left subplot, respectively. In Figure 9a, lower right subplot, we report the (absolute) error map $Err = |\theta_{ob}(x, y) - \theta^*(x, y, T)|$, its maximum value is $maxerr = 0.9935$ attained in few spatial zones of the data map. This can be quantified by estimating the relative errors in Frobenius norm of the first guess and of the optimal pattern, that are given by relerr$_0$ = 0.5478 and relerr* = 0.4895, respectively, showing that a slight improvement is indeed obtained. The convergence history of the optimization procedure is reported in Figure 9b: in the middle subplot we show the convergence of the PIP cost function $J(C, B)$ and in the right subplot we show the corresponding convergence of the gradient norm. Since for this cost function there is only one zone of low values, the problem is well-posed (condition number of order 20) and

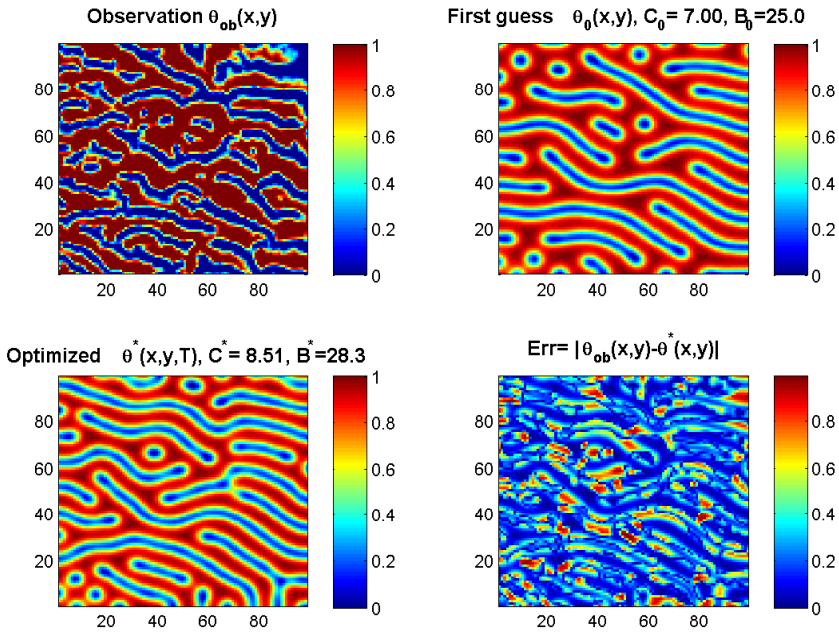

(a) Top line: true data map (left); first guess $\theta_0(x, y, T)$ for the optimization starting from $(C_0, B_0) = (7, 25)$. Bottom line: optimal pattern obtained for $(C^*, B^*) = (8.5096, 28.2614)$ (left); absolute error map Err (right) wrt the data, its maximum is $maxerr = 0.9935$, while the relative errors of the first guess and of the optimal pattern are $\text{relerr}_0 = 0.5478$, $\text{relerr}^* = 0.4895$

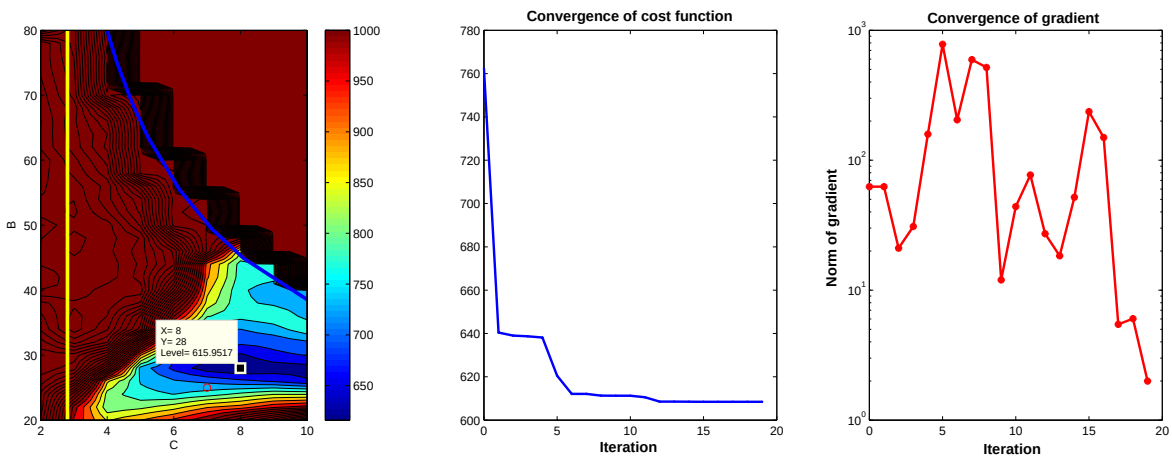

(b) From left to right: contours of cost function; convergence of the cost function; convergence of the norm of the gradient

Figure 9. R_3- reversed spots& worms

the minimization converges with or without regularization.

6.4. *R_4- reversed spots (holes)*

In this example, the data map $M_4 \in R^{N\times N}$, $N = 100$ pixels correspond to original data, so in the PIP problem we have again $N_x = N_y = 100$. The sample is an ASTM A705 Type 630 (17-4 PH

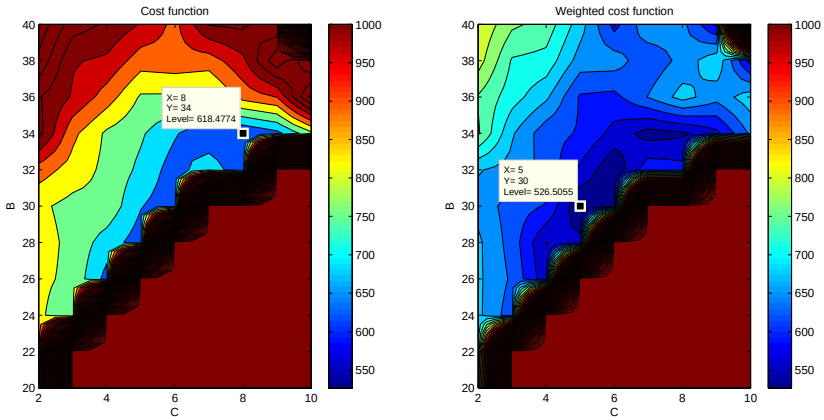

(a) Left: Unweighted PIP cost function $J(C, B)$. Right: Weighted PIP cost function $J(C, B)$.

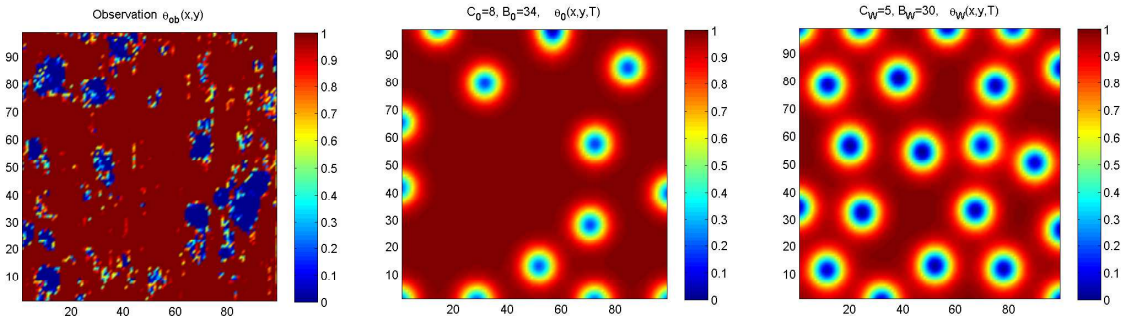

(b) Left: true data map M_4. Middle: pattern $\theta_0(x, y, T)$ corresponding to the *unweighted* minimum $(C_0, B_0) = (8, 34)$ of the cost function in Figure 10a, left. Right: pattern $\theta_W(x, y, T)$ for the *weighted* minimum $(C_W, B_W) = (5, 30)$ in Figure 10a, right. The corresponding relative errors in Frobenius norm are $\text{relerr}_0 = 0.3797$ and $\text{relerr}_W = 0.4112$, respectively.

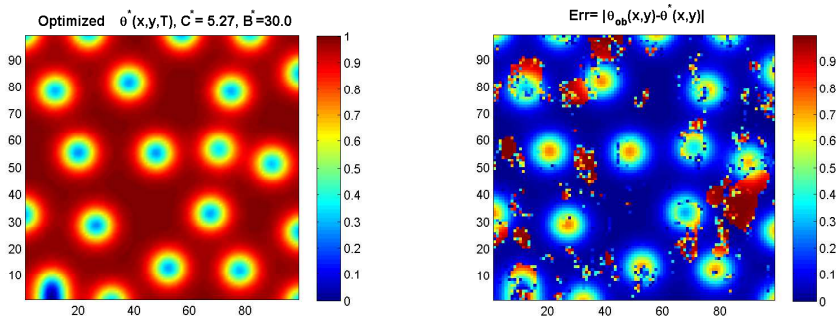

(c) Left: optimal solution $\theta^*_W(x, y, T)$ of weighted PIP for $(C^*_W, B^*_W) = (5.2665, 29.9633)$ obtained starting the minimization algorithm by $(C_W, B_W) = (5, 30)$. Right: Corresponding absolute error map Err, the relative error in Frobenius norm is now $\text{relerr}^*_W = 0.3797$.

Figure 10. R_4-reversed spots (holes)

precipitation hardening martensitic stainless steel) coupon, tested for pitting resistance according to the ASTM G61 protocol in 20,000 ppm chloride solution at 60°C. The image has been acquired as an in-plane SEM micrograph. We report the data $\theta_{ob}(x, y) = M_4$ in Figure 10b, left subplot. We fix the value $A_2 = 1$ as in the case of simulated reverse spots reported in Section 5. Nevertheless, here we fix the scaling parameter $\rho = 0.25$, because a few large holes are present in the data. In fact, as outlined in [44], this parameter is related to the effective domain size for pattern selection

and it is able to tune the size of pattern features (e.g. holes/spots dimension, labyrinth width). Moreover, smaller values of ρ imply slower time dynamics in the reaction-diffusion model. For this reason, we consider the final time of integration as $T = 300$ such that a stationary pattern can be attained.

The PIP cost function $J(C, B)$ in (7) calculated on the subdomain $\mathcal{R}$=$[2, 10] \times [20, 40]$ is reported in Figure 10a, left. On the rough meshgrid used for this computation, the minimum is attained at $(C_0, B_0) = (8, 34)$ where $J(C_0, B_0) = 618.4774$. The corresponding pattern $\theta_0(x, y, T)$ is shown in Figure 10b (middle). We note that, a pattern of holes is obtained, but they are in wrong places with respect to the true holes. In part this is due to the fact that we are minimizing in the Frobenius norm. Hence a predicted hole in the wrong location will receive the same weight in the objective function, whether it is close to the true hole or not. Hence, in order to emphasise the fit to the spatial location of the holes, we aim to give more importance to the pixels of the data map where the holes are present (lower absolute values). For this reason, we investigate the use of the data values themselves as the weighting matrix for the cost function in (7). Hence, we choose W as a diagonal matrix with entries dependent on the values of the map M_4, in particular we choose $\text{diag}(W) = (1 + \hat{M}_4^2)^{-1}$. The weighted cost function obtained is reported in Figure 10a, right. On the rough meshgrid used for the computation, the minimum is now attained at $(C_W, B_W) = (5, 30)$ and $J(C_W, B_W) = 526.5055$. The corresponding pattern $\theta_W(x, y, T)$ is shown in Figure 10b (right). Moreover, the relative errors in Frobenius norm of $\theta_0(x, y, T)$ and $\theta_W(x, y, T)$ with respect to the data map are $\text{relerr}_0 = 0.3892$ and $\text{relerr}_W = 0.4112$, respectively.

Starting the optimization of the weighted PIP by $(C_W, B_W) = (5, 30)$, after 12 iterations the algorithms stops at $(C_W^*, B_W^*) = (5.2665, 29.9633)$ with $J(C_W^*, B_W^*) = 520.587$. The corresponding optimal pattern $\theta_W^*(x, y, T)$ and its absolute error map are shown in Figure 10c, on the left and on the right, respectively. The relative error in the Frobenius norm with respect to the data map is reduced to $\text{relerr}_W^* = 0.3797$.

7. Conclusions

In this study we have demonstrated how the approach of parameter estimation can be used to fit a model of morphological electrodeposition to experimental data. Previous work had shown that the model could support many of the different patterns seen in experiments [6, 21]. The work presented here has shown how the model-data comparison can be made in a more quantitative way. In the first part of the study, presented in Section 5, experiments with simulated noisy data not only validated the methodology, but provided a method for objectively dividing the bifurcation diagram of the RD-PDE system into different regions. An examination of the structure of the cost function of the estimation problem for different types of patterns showed well-defined minima in specific regions of parameter space. By examining the structure of these minima we were able to define the zones of the bifurcation diagram corresponding to the different patterns. Thus the methodology presented was able to indicate an appropriate segmentation of the bifurcation diagram.

In the second part of the study, presented in Section 6, the method of parameter estimation was used to fit the RD-PDE model to patterns arising from true experimental data. As for the simulated data, an examination of the structure of the cost function by solving the first step PIP(i) then indicated the area S_T of parameter space where particular patterns could be generated. This was used to provide a good first estimate of the appropriate parameters to generate the pattern seen in the data. Optimization of the cost function in the second step PIP(ii), using a gradient descent method and starting from this first estimate, was then able to retrieve appropriate parameters to produce a PDE model solution that closely fitted the data. As far as we are aware, this is the first

demonstration of objectively fitting an electrodeposition model to such a variety of patterns arising from experiments.

The parameters with respect to which the optimization was performed correspond to well-defined choices within an experiment for metal growth. Thus the method presented here provides an objective tool to begin to guide experimental design to produce a desired pattern. However, this is only a first step towards such a tool. This work could be extended in many ways. Here we have estimated only the two most influential parameters. However, it would also be interesting to estimate other parameters, for example A_2 and ρ, as part of the algorithm. A sensitivity analysis of the different model parameters is currently under study. We could also envisage treating the parameters as functions of time and space, though this implies the need for new analytical studies for the pattern formation problem in this case. For the example of the reversed spots in Section 6.4 we showed that for certain data it was not appropriate to use an identity weighting matrix within the cost function. Here we used a simple weight based on the values of the data, but other weights could be considered. In particular, if something is known about the statistics of the errors in the data, then the variances of these errors could be used as a diagonal weighting matrix, and even covariance information could be used. This may help improve the match to the data values. We have also only considered fitting the RD-PDE model to the surface chemistry θ. In practice we also have measurements of the 3D morphology profile $h(x, y, t)$ in (1) (see for example [27]) and these data could also be used to further constrain the fit.

Furthermore, this study was restricted to the stationary patterns generated within the Turing region. The fitting of non-stationary patterns associated with the Turing-Hopf region presents further challenges associated with the oscillatory nature of the PDE model solutions. A first PIP study with time oscillation data for the ODE morphochemical model has been performed in [30]. The extension of our approach to time and space oscillating patterns will be considered in future research.

Appendix: Numerical approximation of the RD-PDE system

In order to solve the reaction-diffusion PDE system on the 2D spatial domain $\Omega = [0, L_x] \times [0, L_y]$ and for $t \in [0, T]$ we apply the Extended Central Difference Formulas (ECDF) for semi-discretization in space coupled with the Alternating Direction Implicit (ADI) method in time that approximate implicitly the diffusion term and explicitly the reaction terms. ADI-ECDF schemes of order $p = 2, 4, 6$ have been recently introduced in [23] to deal with the approximation of Turing patterns that are stationary solutions of the PDE system in an accurate and efficient way with a flexible choice of integration stepsizes both in space and time. This task is challenging from the computational point of view because high accuracy is required both in space, to capture the pattern structure, and in time, to attain the stationary pattern in a stable way. Moreover, in [60] this approach has been successfully applied to deal with the case of oscillating Turing patterns arising from the superimposition of an external forcing term in the source, representing sinusoidally modulated electrochemical control resulting in a notable smoothing effect. For these reasons in [21], we approximated the model (2)-(3) with zero Neumann boundary conditions for sets of parameters corresponding to Turing and Turing-Hopf regions, where stationary patterns and patterns oscillating in space and time are expected, respectively. Moreover, for parameters in the (green) region indicated in Figure 1, we applied these schemes also in [22] for the numerical approximation of spiral waves. In the main text of this paper, the PDE simulations involved in several steps of optimization algorithm minimizing the PIP cost function (7) have been obtained by using ADI-ECDF with moderate stepsizes both in space and time with consequently reduced computational costs.

Moreover, to allow a more straightforward presentation of the numerical results, in all simulations we calculate two auxiliary quantities:
i) $\|\theta_{r+1} - \theta_r\|_2$: the difference in norm between two consecutive patterns, i.e. the numerical approximations at the times t_{r+1} and t_r along the time integration. This quantity evaluates the tendency of the solution to reach a stationary pattern: in this case this difference should tend to zero (we can stop the time integration when this value is less than an appropriate threshold); for sake of exposition, in this paper we calculated this indicator but we do not report it in the numerical results.
ii) $\langle\theta(t)\rangle$: an approximation of the space integral $\frac{1}{|\Omega|}\int_\Omega \theta(x, y, t)dx\, dy$. This second indicator is a spatial mean value that, for longtime integration, allows us to discriminate between stationary and oscillating patterns. In fact, if $\langle\theta(t)\rangle$ reaches an approximately constant value, a stationary pattern tends to be attained, while an asymptotic oscillatory behaviour of $\langle\theta(t)\rangle$ indicates an oscillating pattern. This indicator has been used in the main text of this paper when it was important to check that the dynamics of the PDE model reached the stationary Turing pattern expected.

Acknowledgements

The authors are grateful to Deborah Lacitignola for useful discussions. We acknowledge the Department of Mathematics and Physics "Ennio De Giorgi" at the University of Salento, Lecce, for supporting a visit of A.S. Lawless. The research work of I.Sgura has been performed under the auspices of the Italian National Group for Scientific Calculus (GNCS-INdAM).

References

[1] Koper MTM. Non-linear phenomena in electrochemical systems. J Chem Soc Faraday Trans. 1998; 94: 1369–1378.
[2] Krischer K, Mazouz N, Grauel P. Fronts, Waves, and Stationary Patterns in Electrochemical Systems. Angew Chem Int Ed. 2001; 40: 850–869.
[3] Li YJ, Oslonovitch J, Mazouz N, et al. Turing-Type Patterns on Electrode Surfaces. Science 2001; 291: 2395–2398.
[4] Dobrovolska Ts, Lopez-Sauri DA, Veleva L, et al. Oscillations and spatio-temporal structures during electrodeposition of Ag-Cd alloys. Electrochim Acta 2012; 79: 162–169.
[5] Krastev I, Dobrovolska Ts, Lacnjevac U, et al. Pattern formation during electrodeposition of indium-cobalt alloys. J Solid State Electrochem, 2012; 16: 3449–3456.
[6] Bozzini B, Lacitignola D, Sgura I. Spatio-temporal organisation in alloy electrodeposition: a morphochemical mathematical model and its experimental validation. J Solid State Electrochem 2013; 17: 467–479, doi: 10.1007/s10008-012-1945-7
[7] Gianoncelli A, Sgura I, Bocchetta P, et al. High-lateral resolution X-ray fluorescence microspectroscopy and dynamic mathematical modelling as tools for the study of electrodeposited electrocatalysts. X-RAY Spectrometry. 2015; 44: 263–275, doi:10.1002/xrs.2617
[8] Dobrovolska Ts, Krastev I, Zabinski P, et al. Oscillations and self-organization phenomena during electrodeposition of silver-indium alloys. Experimental study. Arch Metall Mater. 2011; 56: 645–657.
[9] Krastev I, Koper MTM. Pattern formation during the electrodeposition of a silver-antimony alloy. Physica A. 1995; 213: 199–208.
[10] Saitou M, Fukuoka Y. An Experimental Study on Stripe Pattern Formation of Ag-Sb Electrodeposits. J Phys Chem B. 2004; 108: 5380–5385.

[11] Saitou M, Fukuoka Y. A Study on Transient Changes of Surface Morphologies in Ag and Sb Coelectrodeposition. J Electrochem Soc. 2004; 151: C627–C632. doi: 10.1149/1.1787499
[12] Saitou M, Fukuoka Y. Stripe patterns in Ag-Sb co-electrodeposition. Electrochim Acta. 2005; 50:5044–5049.
[13] Bozzini B, Lacitignola D, Sgura I. A reaction-diffusion model of spatial pattern formation in electrodeposition. J of Physics Conf Series. 2008; 96: 012051. doi:10.1088/1742-6596/96/1/012051
[14] Bozzini B, D'Urzo L, Lacitignola D, et al. An investigation into the dynamics of Au electrodeposition based on the analysis of SERS spectral time series. Trans Inst Met Fin. 2009; 87: 193–200, doi:10.1179/174591909X438929
[15] Bozzini B, Lacitignola D, Sgura I. Morphological spatial patterns in a reaction diffusion model for metal growth. Math Biosc and Engin. 2010; 7: 237 – 258 doi:10.3934/mbe.2010.7.237
[16] Bozzini B, Sgura I, Lacitignola D, et al. Prediction of morphological properties of smart-coatings for Cr replacement, based on mathematical modelling. Adv Mat Res. 2010; 138: 93–106, doi:10.4028/www.scientific.net/AMR.138.93
[17] Bozzini B, Lacitignola D, Sgura I. Travelling Waves in a Reaction-Diffusion Model for Electrodeposition. Math Comp Simul. 2011; 81:1027–1044, doi:10.1016/j.matcom.2010.10.008
[18] Bozzini B, Lacitignola D, Sgura I. Frequency as the greenest additive for metal plating: mathematical and experimental study of forcing voltage effects on electrochemical growth dynamics. Int J Electrochem Sci. 2011; 6:4553–4571.
[19] Bozzini B, Lacitignola D, Mele C, et al. Coupling of Morphology and Chemistry Leads to Morphogenesis in Electrochemical Metal Growth: a Review of the Reaction-Diffusion Approach. Acta Applic Mathematicae. 2012; 122: 53–68. doi: 10.1007/s10440-012-9725-z
[20] Bozzini B, Lacitignola D, Mele C, et al. Morphogenesis in metal electrodeposition. Note di Matem. 2012; 32:7–46. doi:10.1285/i15900932v32n1p7
[21] Lacitignola D, Bozzini B, Sgura I. Spatio-temporal organization in a morphochemical electrodeposition model: Hopf and Turing instabilities and their interplay, Euro J of Applied Mathematics Cambridge Univ Press. 2015; 26:143–173. doi:10.1017/S0956792514000370
[22] Lacitignola D, Bozzini B, Sgura I. Spatio-temporal organization in a morphochemical electrodeposition model: analysis and numerical simulation of spiral waves. Acta Applic Mathematicae. 2014; 132: 377389. doi: 10.1007/s10440-014-9910-3
[23] Sgura I., Bozzini B., Lacitignola D. Numerical approximation of Turing patterns in electrodeposition by ADI methods. J Comp Appl Math. 2012; 236: 4132–4147. doi:10.1016/j.cam.2012.03.013
[24] De Wit A, Lima D, Dewel G, et al. Spatio-temporal dynamics near a codimension-two point. Phys Rev E. 1996; 54: 261–271.
[25] Rudovics B, Dulos E, de Kepper P. Standard and nonstandard Turing patterns and waves in the CIMA reaction. Physica Scripta. 1996; T67: 43–50.
[26] Ricard MR, Mischler S. Turing Instabilities at Hopf Bifurcation. J Nonlinear Sci. 2009; 19: 467–496. doi:10.1007/s00332-009-9041-6
[27] Sgura I, Bozzini B. XRF map identification problems based on a PDE electrodeposition model, J Phys D: Appl Phys. 2017; 50: 154002 doi:10.1088/1361-6463/aa5a1f
[28] Deuflhard P and Roblitz S. *A guide to numerical modelling in systems biology* Vol. 12 2015 Springer
[29] Roblitz S, Stotzel C, Deuflhard P, Jones H M , Azulay D O, van der Graaf P H and Martin S W. A mathematical model of human menstrual cycle for the administration of GnRH analogues. Journal of Theoretical Biology. 2013; 321: 8-27
[30] D'Autilia MC, Bozzini B, Sgura I. Parameter identification in ODE models with oscillatory dynamics: a Fourier regularization approach. Inverse Problems 2017; 33(12):124009 doi: 10.1088/1361-6420/aa9834

[31] Giles MB, Pierce NA. An introduction to the adjoint approach to design. Flow, turbulence and combustion. 2000; 65: 393–415.
[32] Iglesias M, Dawson A. The regularizing Levenberg-Marquardt scheme for history matching of petroleum reservoirs. Comput Geosciences. 2013; 17: 1033–1053.
[33] Navon IM. Practical and theoretical aspects of adjoint parameter estimation and identifiability in meteorology and oceanography. Dynamics of Atmospheres and Oceans. 1998; 27: 55–79.
[34] Pinnington EM, Casella E, Dance SL, et al. Investigating the role of background and observation error correlations in improving a model forecast of forest carbon balance using four dimensional variational data assimilation. Agriculture and Forest Meteorology 2016; 228–229: 299–314.
[35] Blazakis K N, Madzvamuse A, Reyes-Aldasoro CC, et al. Whole cell tracking through the optimal control of geometric evolution laws. J of Computational Physics. 2015; 297: 495–514. doi:10.1016/j.jcp.2015.05.014
[36] Croft W, Elliott C M, Ladds G, et al. Parameter identification problems in the modelling of cell motility. J of Mathematical Biology. 2015; 71: 399-436. doi:10.1007/s00285-014-0823-6
[37] Hogea C, Davatzikos C, Biros G. An image-driven parameter estimation problem for a reaction-diffusion glioma growth model with mass effects. J of Mathematical Biology. 2008; 56: 793-825, doi:10.1007/s00285-007-0139-x
[38] Figueiredo IN, Figueiredo P, Almeida N. Image-driven parameter estimation in absorption-diffusion models of chromoscopy, SIAM Journal on Imaging Sciences 2011. 4, 3: 884–904, doi.org/10.1137/100798405
[39] Isabel N. Figueiredo I N, Carlos Leal C. Physiologic Parameter Estimation Using Inverse Problems. SIAM Journal on Applied Mathematics 2013. 73, No. 3: 1164–1182, doi.org/10.1137/120866403
[40] Garvie MR, Maini PK, Trenchea C. An efficient and robust numerical algorithm for estimating parameters in Turing systems. J of Computational Physics. 2010; 229: 7058–7071. doi:10.1016/j.jcp.2010.05.040
[41] Garvie MR, Trenchea C. Identification of Space-Time Distributed Parameters in the Gierer–Meinhardt Reaction-Diffusion System. SIAM J on Applied Mathematics. 2014; 74: 147–166. doi: 10.1137/120885784
[42] Stoll M, Pearson J W, Maini PK. Fast solvers for optimal control problems from pattern formation. J of Computational Physics. 2016; 304: 27–45. doi:10.1016/j.jcp.2015.10.006
[43] Lacitignola D. Bifurcations of equilibria in a mathematical model for metal growth. Atti dell'Accademia Peloritana dei Pericolanti- Classe di Scienze Fisiche, Matematiche e Naturali, ISSN: 1825-1242, 2018 to appear
[44] Lacitignola D, Bozzini B, Sgura I, et al. Turing pattern formation on the sphere for a morpho-chemical electrodeposition model. Commun Nonlinear Sci Numer Simulat. 2017; 48: 484-508 doi:10.1016/j.cnsns.2017.01.008
[45] Lacitignola D, Bozzini B, Peipmann, Sgura I. Cross-diffusion effects on a morpho-chemical model for electrodeposition. Applied Mathematical Modelling. 2018; 57:492-513 doi:10.1016/j.apm.2018.01.005
[46] Bozzini B, Amati M, Gregoratti L, et al. Intermetallics as key to spiral formation in In-Co electrodeposition. A study based on photoelectron microspectroscopy, mathematical modelling and numerical approximations. J Physics D: Appl. Physics. 2015; 48: 395502 (12pp) doi: 10.1088/0022-3727/48/39/395502
[47] Anita S, Arnautu V, Capasso V. An introduction to optimal control problems in life sciences and economics, Birkhauser Eds. 2011
[48] Lenhart S, Workman J, Optimal control applied to biological models, Mathematical and Computational Biology Series, London, Chapman & Hall/CRC, 2007.
[49] Tarantola A. Inverse problems theory and methods for model parameter estimation. Philadel-

phia SIAM 2005. ISBN 0-89871-572-5
[50] Hansen PJ. Rank-deficient and discrete ill-posed problems: numerical aspects of linear inversion. SIAM 1998. ISBN: 978-0-898714-03-6
[51] Mead J L. Discontinuous parameter estimates with least squares estimators Applied Mathematics and Computation. 2013; 219: 5210–5223.
[52] Mead, J. L., Hammerquist, C. C. χ^2 Tests for the choice of the regularization parameter in nonlinear inverse problems. SIAM Journal on Matrix Analysis and Applications. 2013; 34(3): 1213–1230
[53] Gazzola, S., Reichel, L. A new framework for multi-parameter regularization. BIT Numerical Mathematics. 2016; 56(3): 919–949.
[54] Nocedal J. and Wright SJ. Numerical optimization, Springer-Verlag New York 1999
[55] Lawless AS. Variational data assimilation for very large environmental problems. In Large Scale Inverse Problems: Computational Methods and Applications in the Earth Sciences (2013), Eds. Cullen MJP, Freitag MA, Kindermann S, Scheichl R. Radon Series on Computational and Applied Mathematics 13. De Gruyter, 55–90. 2013
[56] Giering R. and Kaminski T., Recipes for Adjoint Code Construction, ACM Trans. On Math. Software. 1998; 24: 437-474.
[57] Golub G. H. and Van Loan C. F. (1996). Matrix computations. Johns Hopkins University Press, Baltimore, MD, USA.
[58] Bozzini B, Bocchetta P, Alemàn B, Amati M, Gianoncelli A, Gregoratti L, Sezen H, Taurino A and Kiskinova M. Electrodeposition and pyrolysis of Mn/polypyrrole nanocomposites: a study based on soft X-ray absorption, fluorescence and photoelectron microspectroscopies. J. Mater. Chem. A. 2015; 3: 19155–19167
[59] Bozzini B., Kourousias G., Bedolla D.E., Gianoncelli A. Chemical-state evolution of Ni in Mn-Ni/polypyrrole nanocomposites under bifunctional air electrode conditions, investigated by quasi-in situ multi-scale soft X-ray absorption spectroscopy. Materials Today Energy. 2017; 6: 154–163
[60] Sgura I., Bozzini B., Lacitignola D. Numerical approximation of oscillating Turing patterns in a reaction-diffusion model for electrochemical material growth. AIP Conference Proceedings. 2012; 1493: 896–903. doi: 10.1063/1.4765594